inner core growth, which should preserve radial symmetry. They are reminiscent of what one might expect to observe if large-scale low-order convection were the dominant cause of anisotropy in the inner core (Fig. 4D). This model is oversimplified and is only shown for qualitative comparison. Note, however, that the range of predicted velocities is in good agreement with that obtained by inversion. In a convecting inner core, anisotropic effects of crystal alignment are expected to dominate over lateral heterogeneity due to density anomalies (*12*, *17*).

Mode 1 convection (Fig. 4, D and E) is not necessarily the dominant mode of convection in the inner core. The longitudinal averaging inherent in our modeling, the limited parameterization, errors in the data due to unmodeled mantle effects, and possible lateral heterogeneity in the inner core prevent us from further characterization of these patterns. However, since anisotropy extends to the center of the inner core (*10*), the likelihood of low-order convection is supported by numerical computations (*17*), which indicate that high Rayleigh number chaotic solutions would tend to concentrate effects detectable by means of anisotropy at shallow depths in the inner core. A physical explanation for why a low-order convection pattern in the inner core should align with the Earth's rotation axis remains to be found (*30*).

REFERENCES AND NOTES

1. J. H. Woodhouse, D. Giardini, X. D. Li, *Geophys. Res. Lett.* **13**, 1549 (1986); A. Morelli, A. M. Dziewonski, J. H. Woodhouse, *ibid.*, p. 1545. There are several branches of core penetrating *P* waves. PKP(DF) goes through the inner core, whereas PKP(BC) and PKP(AB) remain in the liquid outer core, assumed to be homogeneous. BC and AB are observed at distances for which DF samples the outer third and inner two thirds of the inner core, respectively.
2. G. Poupinet, R. Pillet, A. Souriau, *Nature* **305**, 204 (1983).
3. G. Masters and F. Gilbert, *Geophys. Res. Lett.* **8**, 569 (1981). Aspherical structure and anisotropy break the azimuthal degeneracy of free oscillations, leading to separation of a mode of angular order *l* into $(2l + 1)$ singlets.
4. P. M. Shearer, K. M. Toy, J. A. Orcutt, *Nature* **333**, 228 (1988).
5. X. Song and D.V. Helmberger, *Geophys. Res. Lett.* **20**, 2591 (1993).
6. P. M. Shearer, *J. Geophys. Res.* **99**, 19647 (1994).
7. W. Su and A. M. Dziewonski, *ibid.* **100**, 9831 (1994).
8. K. C. Creager, *Nature* **356**, 309 (1992).
9. J. Tromp, *ibid.* **366**, 678 (1993).
10. L. Vinnik, B. Romanowicz, L. Breger, *Geophys. Res. Lett.* **21**, 1671 (1994); X. D. Song, *J. Geophys. Res.* **101**, 16089 (1996).
11. D. J. Doornbos, *Geophys. J. Ry. Astron. Soc.* **38**, 397 (1974); D. R. Fearn, D. E. Loper, P. H. Roberts, *Nature* **292**, 232 (1981).
12. R. Jeanloz and H. R. Wenk, *Geophys. Res. Lett.* **15**, 72 (1988).
13. L. Stixrude and R. E. Cohen, *Science* **267**, 1972 (1995).
14. A. Souriau and B. Romanowicz, *Geophys. Res. Lett.* **23**, 1 (1996); *Phys. Earth. Planet. Inter.*, in press.
15. V. Cormier, *Eos* **75**, 67 (1994).
16. P. Weber and P. Machetel, *Geophys. Res. Lett.* **19**, 2107 (1992).
17. S. Karato, *Science* **262**, 1708 (1993).
18. M. Ritzwoller, G. Masters, F. Gilbert, *J. Geophys. Res.* **91**, 10203 (1986).
19. W. J. Su, R. L. Woodward, A. M. Dziewonski, *ibid.* **99**, 6945 (1994); S. Johnson, P. Shearer, G. Masters, *Eos Fall Suppl.* **75**, 475 (1994).
20. X. D. Li and B. Romanowicz, *J. Geophys. Res.* **101**, 22245 (1996).
21. X. D. Li, thesis, Harvard University (1990); ———, D. Giardini, J. H. Woodhouse, *J. Geophys. Res.* **96**, 551 (1991).
22. R. Widmer, G. Masters, F. Gilbert, *Geophys. J. Int.* **111**, 559 (1992).
23. Bolivia: 9 June 1994, depth = 647 km, moment magnitude (*Mw*) = 8.2; Kurile Islands: 10 October 1994, depth = 68 km, *Mw* = 8.3; J. Tromp and E. Zanzerkia, *Geophys. Res. Lett.* **22**, 2297 (1995); J. S. Resovsky and M. Ritzwoller, *ibid.*, p. 2301; J. Tromp, *Geol. Soc. Am. Today* **5**, 137 (1995).
24. The travel time data set comprises representative subsets of antipodal PKP(AB)-PKP(DF) data from (*10*) and of PKP(BC)-PKP(DF) data from (*14*). The mode data set consists of splitting coefficients *C*00, *C*20, and *C*40, as defined in equation 11 of (*25*), for 19 inner core–sensitive modes, measured using Bolivia and Kurile data only (*23*), and corrected for rotation, ellipticity as well as mantle effects, using (*20*). These coefficients are combined in a spherical harmonic expansion to define the splitting function, and represent integrated effects on the modes of structure from the Earth's center to the surface. Units are in ‰ of degenerate frequency of each mode. The modes considered are given in Table 2. We compared corrections for mantle structure with the use of different mantle models and found that changing the model has no significant effects on our results. Uncertainties on mantle corrections for zonal terms are on the order of 0.1‰. An *S* to *P* wave velocity conversion factor of 0.5 was used in the mantle correction computations. This choice has little effect on the inner core models obtained.
25. D. Giardini, X. D. Li, J. H. Woodhouse, *Nature* **325**, 405 (1987); *J. Geophys. Res.* **93**, 13716 (1988).
26. Models are numbered as follows: #1: $v = 0$, $n = 0$ (constant cylindrical anisotropy with axis parallel to the Earth's rotation axis, 5 parameters); #2: $v = 2$, $n = 0$; #3: $v = 4$, $n = 0$ (cylindrical anisotropy as before, with depth variation allowed in powers of r, up to r^v; 10 and 15 parameters, respectively); #4, $v = 4$, $n = 2$; (35 parameters); #5, $v = 4$, $n = 4$ (both spatial and depth variations are allowed, and the anisotropy need not be cylindrical; the number of free parameters in this case is 44).
27. The determination of the splitting coefficients is a highly nonlinear process. For some inner core–sensitive modes (13S2 and 3S2 in particular), and with the current data set, the solution space exhibits several minima, with significantly different values of the *C*20 and *C*40 terms (for example, Megnin and Romanowicz, *Eos Fall Suppl.* **76**, 46 (1995). We have verified that our solutions remain stable when we remove one or both of these modes. This is particularly important for 3S2, whose splitting dominates the mode data set (Fig. 3).
28. A. M. Dziewonski and D. L. Anderson, *Phys. Earth. Planet. Inter.* **25**, 297 (1981).
29. Previous studies have documented that the top 100 km of the inner core has little anisotropy [(*6*) and X. Song and D. Helmberger, *J. Geophys. Res.* **100**, 9805 (1995)]. Our limited parameterization with depth does not allow us to resolve this level of detail. Future studies should consider depth parameterizations in terms of layers or other local basis functions, but the price to pay will be the loss of the elegance of the formalism.

30. We thank X. Song for making his data available to us and P. Olson for helping us with the computations of streamlines for mode 1 convection, as well as two anonymous reviewers whose comments helped improve the manuscript. This research was partially supported by NSF grant EAR9417862. It is Seismographic Station contribution #9609.

6 May 1996; accepted 8 October 1996

Three-Dimensional Imaging of Single Molecules Solvated in Pores of Poly(acrylamide) Gels

Robert M. Dickson, D. J. Norris, Yih-Ling Tzeng, W. E. Moerner*

Individual fluorescent molecules and individual singly labeled proteins were observed in the water-filled pores of poly(acrylamide) gels by far-field microscopy. Brownian motion was markedly reduced by the gel framework, thus enabling extended study of single fluorophores in aqueous environments. A highly axially dependent laser field was used both to excite the fluorophores and to image the molecules in three dimensions. Single molecules were followed as they moved within and through the porous gel structure. In contrast to dry polymeric hosts, these water-based gels may form a useful medium for single-molecule studies of biological systems in vitro.

Since the first reports of optical detection of single small molecules (*1*–*3*), an important goal has been to address chemical and biological problems with the unique local environmental sensitivity that single molecules provide. One promising technique is the observation of single-fluorophore emission in flowing streams (*4*, *5*) or the use of confocal microscopy (*6*) to detect molecules directly in solution. These techniques have demonstrated their powerful analytical utility for identification of fluorophore-labeled biomolecules; for example, the detection of individual DNA strands both in solutions (*7*) and during

R. M. Dickson, D. J. Norris, W. E. Moerner, Department of Chemistry and Biochemistry, Mail Code 0340, University of California, San Diego, 9500 Gilman Drive, La Jolla, CA 92093–0340, USA.
Y.-L. Tzeng, Scripps Research Institute, 10666 North Torrey Pines Road, La Jolla, CA 92037, USA.

*To whom correspondence should be addressed.

capillary electrophoresis (*8*) was achieved by observing fluorophores diffuse through the focal volume.

Although low-temperature imaging has produced exciting results (*9*), ambient single-fluorophore microscopy has only recently begun to address chemical and biological questions. Examples include imaging of single fluorophores bound in two-dimensional lipid bilayers (*10*) and distance determination between two chromophores on a single surface-bound poly(peptide) (*11*). Because extracting detailed information requires that the fluorophore be localized long enough for the interaction of interest to be observed multiple times, the success of these experiments arose in large part from the spatial confinement of the molecules studied. Other experiments have detected and imaged individual fluorophores immobilized in solid hosts or on surfaces. Similar to the low-temperature work, useful information about the molecules and their local environments was obtained (*12–18*). Liquid-helium temperatures, dry surfaces, and nonaqueous polymers, however, are incompatible with most biological systems. A central challenge, therefore, is to develop more biologically amenable single-fluorophore detection methodologies that facilitate prolonged biochemical or biophysical study. In one recent example, diffusion was reduced by indirect attachment of the fluorophore-labeled biomolecule to a surface (*19*).

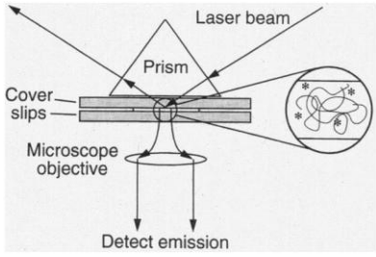

Fig. 1. Apparatus schematic for TIR excitation of fluorophores in PAA gels trapped between two cover slips. The CW laser source was either a 532-nm laser (nile red) or a 632-nm laser (Cy-5 fluorophore). (**Inset**) The random cross-linked gel. The labeled proteins or single fluorophores (asterisks) were isolated in the water-filled spaces between the polymer chains.

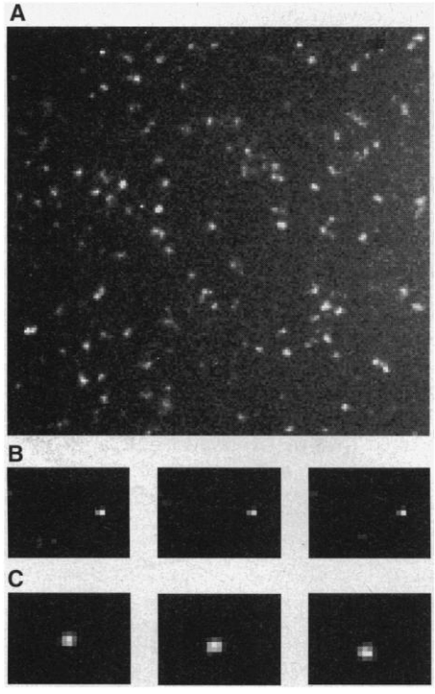

Fig. 2. (**A**) Fluorescence image of single nile red molecules in an 18% PAA gel over a spatial field of 43 μm by 41 μm with ~200-nm resolution with a 1-s exposure time. Emission was collected with an inverted microscope (Nikon) and a cooled Si CCD (Princeton Instruments). (**B**) Three successive expanded images of a molecule fixed in spatial position from frame to frame. (**C**) Three successive expanded images of a molecule moving in position from frame to frame.

In the hope of opening more areas of biophysics to single-molecule studies, we have used as a host matrix the easily manipulated poly(acrylamide) (PAA) gels, which polymerize into cross-linked matrices. Depending on the acrylamide and cross-linker concentrations, the pores enhouse water-filled cavities ranging in diameter from 2 to several hundred nm (*20–22*). Thus, these gels, used routinely as sieves to separate proteins by molecular weight, provide a candidate matrix for restricting the motion of water-soluble molecules, while allowing the molecules to retain solution-based behavior.

To study single fluorophores in the pores of PAA gels, we prepared samples containing 10^{-10} M nile red in deoxygenated aqueous acrylamide–methylenebisacrylamide solution according to standard sodium dodecyl sulfate gel preparation methods (catalysts: tetramethylenediamine and ammonium persulfate) (*23*, *24*). Each sample consisted of a 2-μl aliquot that polymerized rapidly between glass cover slips and remained optically transparent. Even high-concentration PAA gels consist of interconected pores that allow small molecules to diffuse through. The nile red molecules observed in this study were observed in 18 weight % acrylamide gels with 5 weight % cross-linker, yielding average pore diameters of ~2 nm (*20*).

The fluorophore-doped gels were excited with the well-known evanescent wave generated by total internal reflection (TIR) of a 532-nm continuous wave (CW) laser at the cover slip–gel boundary (Fig. 1). The evanescent field intensity, I, falls off exponentially with distance z from the interface, as (*25*)

$$I = I_0 \exp\left[-\frac{4\pi n z}{\lambda}\left(\left(\frac{\sin\theta}{\sin\theta_0}\right)^2 - 1\right)^{1/2}\right] \quad (1)$$

where I_0 is the field intensity at the cover slip–gel interface, λ is the vacuum wavelength, n is the refractive index of the less optically dense medium, and θ and θ_0 are the experimental angle of incidence and the critical angle giving TIR, respectively. In our experiments, the exponential decay length was 125 nm; hence, only a thin layer of material close to the interface was excited. The chief advantage of TIR is that the volume capable of producing background is greatly reduced (*19*). The emitted fluorescence was filtered and observed as in Fig. 2A.

For many images similar to those shown in Fig. 2A, most of the bright spots exhibited transverse (x-y) and axial (z) motion from frame to frame (Fig. 2C). A few single molecules were immobilized in the gel matrix in extremely small pores (Fig. 2B). As confirmation that these stationary bright spots were single molecules, the observed signals remained essentially constant from frame to frame, then suddenly and permanently fell to the background level ("digital" bleaching), resulting from an irreversible photochemical reaction

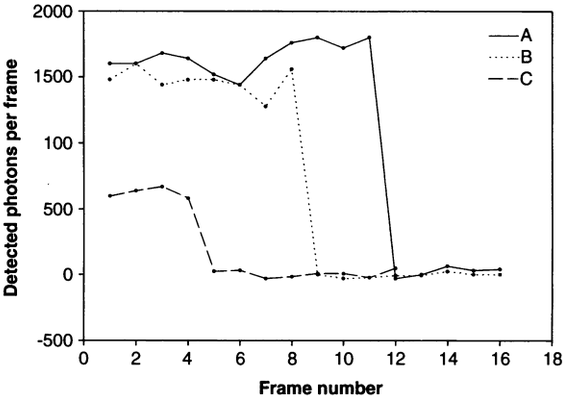

Fig. 3. Detected photons from three representative nile red molecules in 100-ms frames, excited with an intensity of 5 kW/cm^2 at the cover slip–gel interface. These molecules were spatially fixed in the PAA matrix and illustrate digital photochemical bleaching with a bleaching quantum yield of ~10^{-6}. The differences in signal intensity from these three molecules arise from a combination of different dipole-laser polarization alignments and evanescent field intensities (different axial positions).

(Fig. 3). In separate measurements with fixed molecules, the expected strong polarization anisotropy of the absorption was also confirmed.

The TIR excitation scheme provides a three-dimensional (3D) imaging technique by making use of the exponential fall-off in excitation intensity to determine the distance of the fluorophore from the interface. We assume that the transition dipole samples all orientations relative to the excitation polarization during the observation time. In solution at room temperature, this assumption holds very well, because the rotational period is approximately 10^{-9} s (*26*). Hence, the total number of detected photons from a molecule during an exposure can be used as a measure of the local laser intensity, producing a relative distance measurement by inversion of Eq. 1 (*27*). Thus, using TIR at a glass/solution interface enables 3D imaging over the entire disk-shaped focal volume of 120 μm by 120 μm by 250 nm.

In contrast to the spatially fixed molecules, most of the molecules observed in these gels move dramatically, diffusing into and out of the field of view, staying for one to two frames, then disappearing. A subset of the moving molecules (~2%) remained visible for several frames, simultaneously defocusing and losing brightness, and it is the motion of these that we analyze. If a molecule emitted the same number of photons in each frame, drifting out of the focal plane would merely spread these photons over more charge-coupled device (CCD) pixels, leaving the total (spatially integrated) signal unchanged. However, in our experiments, the integrated signal from a given bright spot changed substantially from frame to frame while staying in focus. This result is consistent with the evanescent field intensity being reduced by a factor of 8 for z motion of the molecule by one focal depth (~250 nm). Using the integrated signal from individual bright spots from successive frames, we obtained 3D trajectories for individual molecules (Fig. 4). The strong distance dependence of the evanescent field, which allows the 3D imaging of these molecules, simultaneously biases our measurements in the z direction. We can only analyze molecules that linger in the focal volume for several successive frames, meaning that the axial (z) motion must remain very small (on the order of 200 nm, such that the evanescent field retains sufficient intensity to excite the molecules); therefore, only the transverse motion is analyzed in detail.

Simple Brownian motion requires a single nile red molecule to exhibit mean-square displacement of 900 μm^2 in a 1-s interval, t, according to the expression $\langle x^2 \rangle = (kT/3\pi\eta a)t$, where k is Boltzmann's constant, T is the absolute temperature, η is the solvent viscosity, and a is the molecular radius. We obtained average squared displacements ($\langle x^2 \rangle$ and $\langle y^2 \rangle$) by following 16 different single molecules (Table 1). The 3D trajectories (Fig. 4) and the mean-square displacements (Table 1) indicate that the gel matrix hinders the Brownian motion of single molecules. The discrepancy between observed motion and theoretical Brownian motion occurred for all the molecules studied. For 1-s exposures, the distance traveled was reduced by a factor of ~100 [or, equivalently, the diffusion constant $D = (kT/6\pi\eta a) = \langle x^2 \rangle/2t$ was reduced by a factor of 10^4] in each dimension by the presence of the porous gel matrix. We also found that the average mean-square excursions for longer exposures (1 s) and those for shorter exposures (0.1 s) with a frame rate four times as high were essentially equal. This failure of the mean-square displacement to scale with time is consistent with the observed strong departure from Brownian behavior, thus making these PAA gels suitable for long-time observation of single molecules in solution. Whether or not the motion of the molecules is Brownian between wall encounters, however, poses a difficult experimental problem that requires short-time information. The distances traversed by the observed molecules would occur as a result of simple Brownian motion in only 150 μs, a much faster time than present single-molecule imaging methods are capable of measuring (*10*).

To illustrate the utility of PAA gels for studying singly labeled proteins in aqueous environments, we isolated and imaged singly labeled goat antibodies to rabbit immunoglobulin G (IgG) in 5% PAA gels, which should have pores large enough to accommodate the antibodies (*20*, *28*). Digital bleaching of the Cy-5 fluorophore confirmed that we observed single antibodies. Unlike the free small-molecule fluorophores, however, the labeled proteins re-

Table 1. Mean-square displacements of single molecules in successive exposures at two different data acquisition rates.

1-s exposures at 0.4 Hz*			0.1-s exposures at 1.5 Hz*		
Molecule	$\langle x^2 \rangle$ (μm^2)	$\langle y^2 \rangle$ (μm^2)	Molecule	$\langle x^2 \rangle$ (μm^2)	$\langle y^2 \rangle$ (μm^2)
D	0.0893	0.214	L	0.333	0.125
E	0.0536	0.259	M	0.0714	0.286
F	0.0417	0.0729	N	0.125	0.125
G	0.135	0.0521	O	0.286	0.179
H	0.0625	0.0750	P	0.200	0.100
I	0.0938	0.281	Q	0.125	0.125
J	0.0781	0.219	R	0.179	0.143
K	0.292	0.125	S	0.107	0.0714
Mean ± SD	0.105 ± 0.075	0.162 ± 0.085		0.178 ± 0.085	0.144 ± 0.061

*Typically, six frames were used for each mean-square measurement.

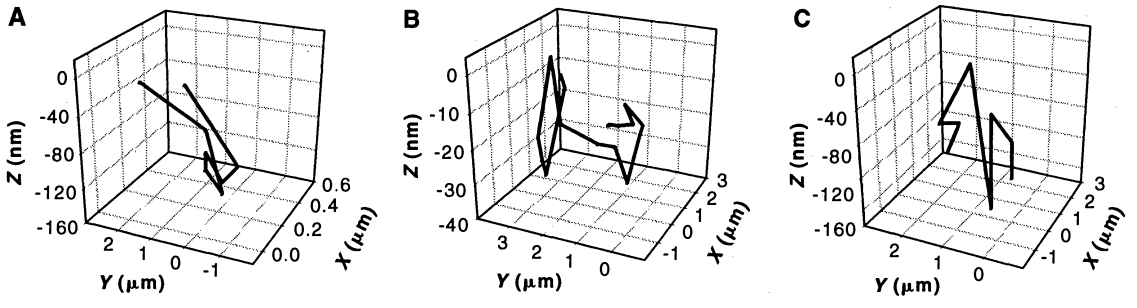

Fig. 4. Three-dimensional trajectories of three separate nile red molecules in 18% PAA gels. (**A** and **B**) The 3D trajectories of two separate molecules obtained from successive 1-s exposures. (**C**) The three-dimensional trajectory obtained with 100-ms exposures. Molecules A and C moved out of the focal volume after 8 frames, whereas molecule B lingered for 15 frames. X and Y distances are in micrometers, Z distances in nanometers. Errors in locating the molecular positions were ~0.1 μm in X and Y, and ~16% of the observed Z position. The zero of the Z axis is defined as the closest approach to the cover slip–gel boundary; motion away from this interface is negative.

mained completely stationary in space, but still exhibited intensity fluctuations of up to 40%. Because individual small fluorophores locked in the gel matrix yielded stable intensities (Fig. 3), we tentatively interpret these amplitude fluctuations as resulting from slow orientational changes of the fluorophore relative to the laser polarization. The motion of the fluorophore label is likely to be hindered by the gel matrix and the nearby protein conformation.

Our experiments indicate that PAA gels offer promise as hosts for single-molecule studies of biological systems. Ease of preparation and controllable pore size make this host material a particularly flexible matrix that should facilitate the study of singly labeled proteins, electrophoresis (29), and individual reactions in solutions. For small fluorophores like nile red, gels as hosts hinder the distance traveled as a result of Brownian motion by approximately two orders of magnitude in each direction for observations on the order of 1 s. This observation means that the signal from any one solvated molecule is concentrated in 1/10,000th of the area of a similar molecule in free solution, thus providing a large increase in detectability solely from the use of the PAA matrix. Although biased in the axial direction, the use of the evanescent field generated by TIR has yielded 3D trajectories of single molecules in solution (30).

REFERENCES AND NOTES

1. W. E. Moerner and L. Kador, *Phys. Rev. Lett.* **62**, 2535 (1989).
2. M. Orrit and J. Bernard, *ibid.* **65**, 2716 (1990).
3. For a review, see W. E. Moerner, *Science* **265**, 46 (1994).
4. E. B. Shera, N. K. Seitzinger, L. M. Davis, R. A. Keller, S. A. Soper, *Chem. Phys. Lett.* **174**, 553 (1990).
5. C. W. Wilkerson, P. M. Goodwin, W. P. Ambrose, J. C. Martin, R. A. Keller, *Appl. Phys. Lett.* **62**, 2030 (1993).
6. M. Eigen and R. Rigler, *Proc. Natl. Acad. Sci. U.S.A.* **91**, 5740 (1994).
7. S. Nie, D. T. Chiu, R. N. Zare, *Science* **266**, 1018 (1994).
8. B. B. Haab and R. A. Mathies, *Anal. Chem.* **67**, 3253 (1995).
9. F. Guttler, T. Irngartinger, T. Plakhotnik, A. Renn, U. P. Wild, *Chem. Phys. Lett.* **217**, 393 (1994); J. Jasny *et al.*, *Rev. Sci. Instrum.* **67**, 1425 (1996).
10. Th. Schmidt, G. J. Schutz, W. Baumgartner, H. J. Gruber, H. Schindler, *Proc. Natl. Acad. Sci. U.S.A.* **93**, 2926 (1996).
11. T. Ha *et al.*, *ibid.*, p. 6264.
12. E. Betzig and R. J. Chichester, *Science* **262**, 1422 (1993).
13. J. K. Trautman, J. J. Macklin, L. E. Brus, E. Betzig, *Nature* **369**, 40 (1994).
14. W. P. Ambrose, P. M. Goodwin, J. C. Martin, R. A. Keller, *Science* **265**, 364 (1994).
15. X. S. Xie and R. C. Dunn, *ibid.*, p. 361.
16. J. J. Macklin, J. K. Trautman, T. D. Harris, L. E. Brus, *ibid.* **272**, 255 (1996).
17. J. K. Trautman and J. J. Macklin, *Chem. Phys.* **205**, 221 (1996).
18. A. J. Meixner, D. Zeisel, M. A. Bopp, G. Tarrach, *Opt. Eng.* **34**, 2324 (1995).
19. T. Funatsu, Y. Harada, M. Tokunaga, K. Saito, T. Yanagida, *Nature* **374**, 555 (1995); R. D. Vale *et al.*, *ibid.* **380**, 451 (1996).
20. J. S. Fawcett and C. J. O. R. Morris, *Sep. Sci.* **1**, 9 (1966).
21. A. G. Ogston, *Trans. Faraday Soc.* **54**, 1754 (1958).
22. D. Rodbard, in *Methods of Protein Separation*, N. Catsimpoolas, Ed. (Plenum, New York, 1976), vol. 2, pp. 145–218.
23. B. D. Hames and D. Rickwood, Eds., *Gel Electrophoresis of Proteins: A Practical Approach*, (Oxford Univ. Press, New York, ed. 2, 1990).
24. J.-R. Daban, M. Samso, S. Bartolome, *Anal. Biochem.* **199**, 162 (1991); *ibid.*, p. 169.
25. J. D. Jackson, *Classical Electrodynamics* (Wiley, New York, 1975), p. 283.
26. B. J. Berne and R. Pecora, *Dynamic Light Scattering with Applications to Chemistry, Biology, and Physics* (Krieger, Malabar, FL, 1990), pp. 143–149.
27. At a glass/solution boundary, this approximation holds to within 10%; the slight deviation from exponentiality arises from near-field coupling of the dipole radiation into the more optically dense glass. See, for example, D. Axelrod and E. H. Hellen, in *Fluorescence Microscopy of Living Cells in Culture, Part B*, D. L. Taylor and Y.-L. Wang, Eds. (Academic Press, San Diego, CA, 1989), pp. 399–416.
28. A. Feinstein and A. J. Rowe, *Nature* **205**, 147 (1965).
29. B. H. Zimm and O. Lumpkin, *Macromolecules* **26**, 226 (1993).
30. Assuming a Gaussian distribution of molecular displacements, the mean-square axial displacement, $\langle z^2 \rangle$, should be equal to $\langle x^2 \rangle$ and $\langle y^2 \rangle$. To correct for the axial bias, we recall that ~2% of the molecules were observed to be in at least four successive frames. Measured $\langle z^2 \rangle$ values for several of these molecules were $\sim 2 \times 10^{-3}$ μm^2. The probability of an axial mean square displacement this small occurring in the distributions defined by the measured $\langle x^2 \rangle$ and $\langle y^2 \rangle$ values (Table 1) is ~2.7%, thus indicating that, within our experimental error, diffusion in axial and transverse directions is equivalent.

31. We thank L. S. B. Goldstein and R. Sakowicz for useful discussions and for the Cy5-labeled antibody, and B. H. Zimm for a critical reading of the manuscript. D. J. N. was supported in part by a National Science Foundation Postdoctoral Fellowship.

29 July 1996; accepted 18 September 1996

Rate Constants for Charge Transfer Across Semiconductor-Liquid Interfaces

Arnel M. Fajardo and Nathan S. Lewis*

Interfacial charge-transfer rate constants have been measured for *n*-type Si electrodes in contact with a series of viologen-based redox couples in methanol through analyses of the behavior of these junctions with respect to their current density versus potential and differential capacitance versus potential properties. The data allow evaluation of the maximum rate constant (and therefore the electronic coupling) for majority carriers in the solid as well as of the dependence of the rate constant on the driving force for transfer of delocalized electrons from the *n*-Si semiconducting electrode into the localized molecular redox species in the solution phase. The data are in good agreement with existing models of this interfacial electron transfer process and provide insight into the fundamental kinetic events underlying the use of semiconducting photoelectrodes in applications such as solar energy conversion.

Charge-transfer rate constants from delocalized carriers in a semiconducting electrode to outer-sphere redox systems in a liquid electrolyte are an important, controversial, and relatively unexplored aspect of photoelectrochemical energy conversion devices (*1–7*). The kinetic behavior of the delocalized electron in the solid transferring to an electron acceptor in the solution phase is a key issue that is not as fully understood as the process of charge transfer between molecular donors and acceptors in the photosynthetic process (*8*) and related model systems (*9*). Research has recently focused on the magnitude of the electronic coupling terms of these interfacial processes, because such quantities are required to estimate the maximum charge-transfer rate constant expected under conditions of optimal exoergicity (*2, 6, 10–12*). Very large charge-transfer rate constants of majority carriers in the semiconductor can lead to substantial levels of recombination and efficiency losses in photoelectrochemical energy conversion devices, whereas very small interfacial rate constants would be undesirable because they could prevent efficient collection of photogenerated minority charge carriers by redox ions in the solution. Experimental measurements of these rate constants have largely been thwarted by the nonideal energetic behavior of stable semiconductor-liquid contacts (*1*) and by the lack of reliable kinetic measurements on stable semiconductor electrodes in contact with outer-sphere redox couples (*2*). Here, we describe measurements of charge-transfer rate constants for *n*-type Si electrodes in contact with a series of viologen acceptors. These data have yielded experimental values for the maximum majority carrier charge-transfer rate constant at optimal exoergicity and for the reorganization energy for charge transfer across these solid-liquid junctions.

Division of Chemistry and Chemical Engineering, California Institute of Technology, Pasadena, CA 91125, USA.

*To whom correspondence should be addressed.

Single-crystal, (100)-oriented *n*-Si electrodes with donor densities N_d of either 7.84×10^{14} or 6.95×10^{15} cm^{-3} were used in